

pubs.acs.org/JACS Article

# III–V Clathrate Semiconductors with Outstanding Hole Mobility: $Cs_8In_{27}Sb_{19}$ and $A_8Ga_{27}Sb_{19}$ (A = Cs, Rb)

Bryan Owens-Baird, Jian Wang, Suyin Grass Wang, Yu-Sheng Chen, Shannon Lee, Davide Donadio, and Kirill Kovnir\*



Cite This: J. Am. Chem. Soc. 2020, 142, 2031-2041



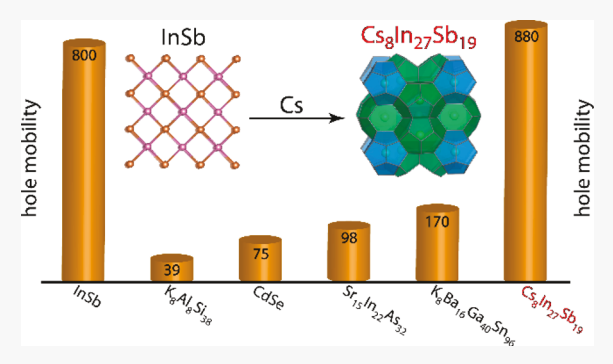
**ACCESS** 

III Metrics & More

Article Recommendations

s Supporting Information

**ABSTRACT:** Three novel unconventional clathrates with unprecedented III—V semiconducting frameworks have been synthesized:  $Cs_8In_{27}Sb_{19}$ ,  $Cs_8Ga_{27}Sb_{19}$ , and  $Rb_8Ga_{27}Sb_{19}$ . These clathrates represent the first examples of tetrel-free clathrates that are completely composed of main group elements. All title compounds crystallize in an ordered superstructure of clathrate-I in the  $Ia\bar{3}$  space group (No. 206; Z=8). In the clathrate framework, a full ordering of {Ga or In} and Sb is observed by a combination of high-resolution synchrotron single-crystal and powder X-ray diffraction techniques. Density functional theory (DFT) calculations show that all three clathrates are energetically stable with relaxed lattice constants matching the experimental data. Due to the complexity of the crystal structure composed of heavy elements, the



reported clathrates exhibit ultralow thermal conductivities of less than 1 W·m<sup>-1</sup>·K<sup>-1</sup> at room temperature. All compounds are predicted and experimentally confirmed to be narrow-bandgap p-type semiconductors with high Seebeck thermopower values, up to  $250~\mu\text{V}\cdot\text{K}^{-1}$  at 300 K for  $\text{Cs}_8\text{In}_{27}\text{Sb}_{19}$ . The latter compound shows carrier concentrations and mobilities,  $1.42\times10^{15}~\text{cm}^{-3}$  and 880 cm<sup>2</sup>·V<sup>-1</sup>·s<sup>-1</sup>, which are on par with the values for parent binary InSb, one of the best electronic semiconductors. The high hole carrier mobility is uncommon for complex bulk materials and a highly desirable trait, opening ways to design semiconducting materials based on tunable III–V clathrates.

#### **■ INTRODUCTION**

The discovery of the first transistor based on Ge revolutionized the electronics device field. Soon after the discovery, it was realized that Ge was not the only choice for semiconductors, and II-VI and III-V materials were intensively investigated in various forms from bulk single crystals down to nanocrystals. 1-5 The III-V proved to be superior than II-VI materials due to higher covalency and substantial carriers mobilities. For example, p-type InSb has a mobility of  $\sim 800 \text{ cm}^2 \text{ V}^{-1} \text{ s}^{-1.6}$ which is comparable to the mobilities of p-type Si (~500 cm<sup>2</sup>  $V^{-1} s^{-1}$ )<sup>7,8</sup> and Ge (~2000–2300 cm<sup>2</sup>  $V^{-1} s^{-1}$ )<sup>9–1</sup>i at similar carrier concentrations. Additionally, III-V materials have been shown to be highly tunable compared to pristine Si and Ge. Due to their outstanding mobilities, binary III-V semiconductors have been used in a number of commercial highprofile electronic applications, such as integrated circuits, LEDs, and high-performance photovoltaics. 12-

Different allotropic modifications for Si and Ge have been reported, including empty clathrate structures, Ge<sub>136</sub> and Si<sub>136</sub>, in which the tetrahedrally coordinated Si or Ge form three-dimensional frameworks with empty polyhedral cages. <sup>18,19</sup> Filling cages in the tetrahedral clathrate frameworks (Figure 1) with various cations, in addition to substituting Si or Ge with elements of groups 10–17, results in over 200 different

clathrate compositions. The mobility of typical Si and Gebased clathrates is lower than that for the elemental semiconductors, for instance,  $4-8~{\rm cm}^2~{\rm V}^{-1}~{\rm s}^{-1}$  for  ${\rm Ba_8Ga_{16}Ge_{30^1}}^{20}$  7 cm² V<sup>-1</sup> s<sup>-1</sup> for  ${\rm Ba_8Al_{16}Si_{30^1}}^{21}$  21 cm² V<sup>-1</sup> s<sup>-1</sup> for  ${\rm Ba_8Cu_{4.61}Ga_{1.04}Ge_{40.35}}^{22}$  39 cm² V<sup>-1</sup> s<sup>-1</sup> for  ${\rm K_8Al_8Si_{38}}^{23}$  50 cm² V<sup>-1</sup> s<sup>-1</sup> for  ${\rm Cs_8Ba_{16}Ga_{40}Sn_{96}}^{24}$  and outstanding report of 170 cm² V<sup>-1</sup> s<sup>-1</sup> for  ${\rm K_8Ba_{16}Ga_{40}Sn_{96}}^{25}$  Clathrates are actively studied because of their thermoelectric, superconducting, and photovoltaic properties. It has been a longstanding goal to design novel clathrates composed of III–V group elements as the framework, leading to significantly higher mobilities that will boost their thermoelectric and photovoltaic potential.

Conventional clathrates, with frameworks composed of tetrel elements of group 14 (Si, Ge, or Sn), can be partially replaced with group 13 triel elements (Al, Ga, or In) to realize the electron-balanced composition, i.e., four electrons per framework atom in the clathrate to achieve tetrahedral

Received: November 15, 2019 Published: January 2, 2020



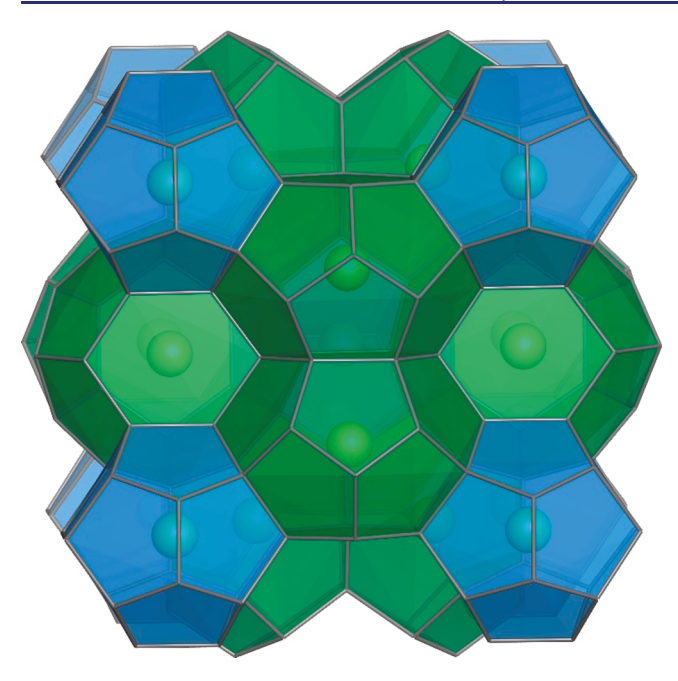


**Figure 1.** Crystal structure of cubic clathrate-I with two types of polyhedral cages emphasized. Pentagonal dodecahedra are shown in blue, and tetrakaidecahedra are shown in green.

coordination. For example, the excess of electrons from K, Cs, or Ba guest cations is compensated with the replacement of tetrel with triel atoms, such as  $Ba_8Ga_{16}Sn_{30}$ , <sup>26</sup>  $Cs_8Ga_8Si_{38}$ , <sup>27</sup>  $K_8In_8Sn_{38}$ , <sup>28</sup> and  $Ba_8Al_{16-x}Si_{30+x}$ . Clathrate frameworks can be made tetrel-free, using transition metals and phosphorus frameworks {Ni,Cu,Zn,Au}-P with Ba, Sr, and La as guest cations, e.g., Ba<sub>8</sub>Cu<sub>16</sub>P<sub>30</sub>, Ba<sub>8</sub>Au<sub>16</sub>P<sub>30</sub>, BaNi<sub>2</sub>P<sub>4</sub>, or SrNi<sub>2</sub>P<sub>4</sub>. To date, few examples of As- or Sb-containing tetrel-free clathrates have been reported: Cs<sub>8</sub>Zn<sub>18</sub>Sb<sub>28</sub>, <sup>39</sup> Rb<sub>8</sub>Zn<sub>18</sub>As<sub>28</sub>, <sup>4</sup> and Ba<sub>8</sub>Cu<sub>16</sub>As<sub>30</sub>. 41 We hypothesized that clathrate frameworks could be composed solely from triels and pnictogens, similar to replacing Ge with GaAs in simple semiconductors. To create a Si- or Ge-free clathrate, two criteria must be met: (i) an electron balance for the composition and (ii) a cation/ framework size match. For example, for clathrate-I structures, with the formula A<sub>8</sub>(In,Sb)<sub>46</sub>, where A is a monovalent alkali guest cation that donates its valence electrons to the framework, the composition A<sub>8</sub>In<sub>27</sub>Sb<sub>19</sub> is electron-balanced.

The total number of available valence electrons is  $1 \times 8(Cs) + 3 \times 27(In) + 19 \times 5(Sb) = 184$ , exactly 4 electrons per 46 framework atoms required for tetrahedral bonding. To select an alkali cation of proper size, the reported tetrel clathrates were analyzed. The triel-antimony frameworks  $In_{27}Sb_{19}$  and  $Ga_{27}Sb_{19}$  have average framework covalent radii of 1.41 and 1.31 Å, respectively. This greatly exceeds the average radii of Si- and Ge-based clathrates ( $\sim$ 1.2 Å) but is comparable to the framework radii of Cs–Sn and Rb–Sn clathrates ( $\sim$ 1.4 Å). Thus, we focused on A–{Ga,In}–Sb systems (A = Rb, Cs). In this work we report the first examples of unconventional clathrates with an entirely III–V framework. Synthesis guided by *in situ* studies, an ordered clathrate superstructure, thermal stability, calculated electronic structure, and outstanding transport properties for the novel clathrates are discussed.

# **■ RESULTS AND DISCUSSION**

**Crystal Structure of Cs**<sub>8</sub>**In**<sub>27</sub>**Sb**<sub>19</sub>. Cs<sub>8</sub>**In**<sub>27</sub>**Sb**<sub>19</sub> crystallizes in the body-centered  $Ia\overline{3}$  space group (No. 206; Z=8) with a unit cell length of a=24.4620(8) Å at 100 K. This  $2a\times 2a\times 2a$  clathrate superstructural unit cell is 8 times larger than the  $Pm\overline{3}n$  archetypical type-I clathrate. In the  $Ia\overline{3}$  structure the 10 framework sites are able to accommodate 27.8=216 In and 19.8=152 Sb atoms without mixed occupancy of the atomic site by elements of different chemical nature. The ordered unit cell has 13 crystallographic positions: 8a, 8b, two 16c, two 24k, and seven 48e sites (Figure 2; Tables S1–S3).

Refinement of the crystal structure of Cs<sub>8</sub>In<sub>27</sub>Sb<sub>19</sub> is challenging because In and Sb have similar X-ray scattering factors, atomic numbers 49 and 51. Both single crystal and powder synchrotron diffraction techniques showed an existence of superstructure with respect to traditional clathrate-I primitive cubic cell (see Supporting Information for details). Synchrotron single crystal X-ray diffraction data set was collected up to high  $\sin\theta/\lambda = 1.19$  and data/parameters ratio of 203, which allow for distinguishing In and Sb sites in the final refinement. After all atomic positions had been found in the initial solution, the assignment of In and Sb within the 10 framework positions followed. Initially, In and Sb were randomly assigned to the sites and the model was refined. Each site occupancy was then allowed to individually refine with the notion that for the incorrectly assigned atom type the site occupancy would rise or lower toward the correct atom type. For instance, an Sb site with site occupancy refined to

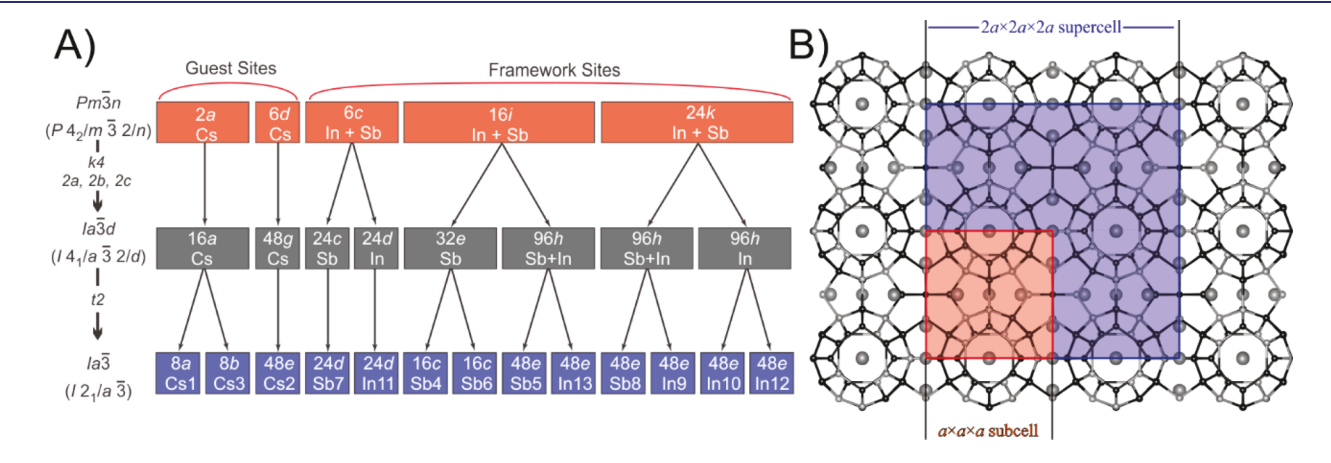


Figure 2. (A) Diagram showing the group—subgroup Wyckoff site splitting from the ideal type-I clathrate  $Pm\overline{3}n$  subcell into the  $Ia\overline{3}$  supercell for  $Cs_8In_{27}Sb_{19}$ . (B) Projection of the clathrate superstructure with subcell and supercell emphasized in orange and blue.

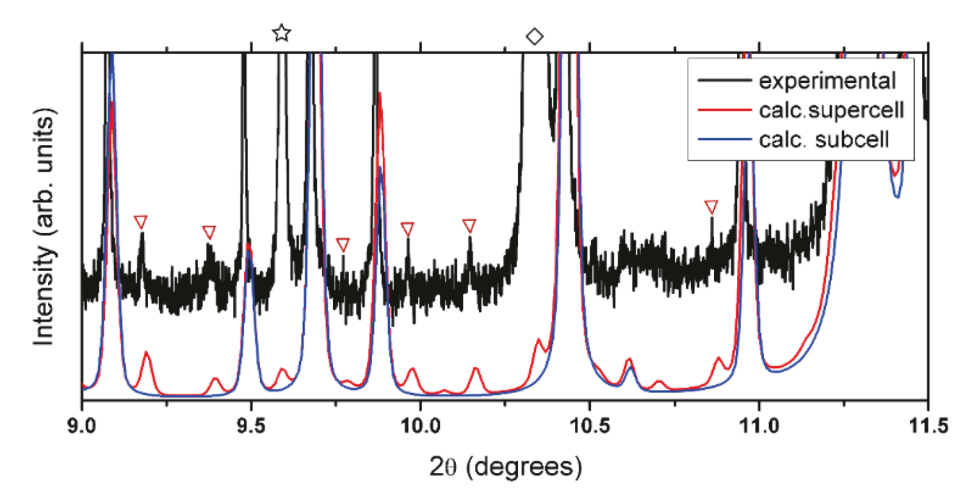


Figure 3. Region of high-resolution synchrotron PXRD pattern for  $Cs_8In_{27}Sb_{19}$  sample collected at room temperature,  $\lambda=0.412.75$  Å. Experimental data (black), calculated pattern for  $Ia\overline{3}$  superstructure (red), and calculated pattern for  $Pm\overline{3}n$  subcell (blue) are shown. Highlighted supercell reflections are denoted by red triangles, while reflections attributed to In and InSb impurity phases are shown as stars and diamonds, respectively. Note that the relative intensity of superstructural reflections does not exceed 0.15%.

0.95(1)-0.97(1) is expected to be In, while a site occupancy refinement that was close to unity within one esd would suggest Sb to be the correct atom type. This analysis was performed with multiple iterations stepwise for each of the 10 framework sites. After the sites were assigned and refined, the last step was to refine each site occupancy again to confirm they refined close to unity. The final model converges to positions with 100% occupancy within one esd and refined composition to be exactly  $Cs_8In_{27}Sb_{19}$ .

Our refinement is unable to distinguish a site that is 100% occupied by an atom of one type from the situation when the site is 90%/10% joint occupied by both In and Sb. There are two arguments supporting full 100% occupancy of each site by atom of one type: (i) an existence of the isostructural Gacontaining clathrates with full Ga/Sb ordering detected due to high scattering contrast of Ga and Sb (vide infra); (ii) an existence of the superstructural ordering. Indeed, a driving force for the superstructural ordering is a preference in chemical bonding, i.e., maximizing In-Sb and minimizing In-In and Sb-Sb interactions in the framework. Otherwise, mixed In/Sb sites can be realized in a primitive  $Pm\overline{3}n$  clathrate subcell, similar to the case of Ba<sub>8</sub>Cu<sub>14</sub>Ge<sub>6</sub>P<sub>26</sub>;<sup>33</sup> in such clathrate framework a random mixture of In-Sb, In-Sn, and Sb-Sb interactions will be present. Four times increase of the primitive cell volume is only necessary for the complete segregation of In and Sb over a distinct framework sites to optimize chemical bonding in the clathrate framework. The predominant interactions present within the  $Ia\overline{3}$  framework are In-Sb bonds, with a few In-In contacts, and finally only one Sb-Sb bond. In-Sb distances range between 2.802 and 2.893 Å with average In-Sb distance of 2.86 Å, slightly elongated compared with the sum of the two covalent radii (In-Sb, 2.81 Å;  $r_{\text{In}} = 1.42$  Å;  $r_{\text{Sb}} = 1.39$  Å)<sup>43</sup> but well in-line with distances reported for A<sub>2</sub>In<sub>2</sub>Sb<sub>3</sub> compounds.<sup>44–46</sup>

The observed In–In distances range between 2.778 Å and 2.847 Å, agreeing well with the double covalent radius of In, 2.84 Å. These are slightly shorter than In–In distances in ternary Zintl phases, such as  $K_{10}In_5Sb_9$  (2.92 Å) and  $Ba_5In_4Sb_6$  (2.85 and 2.97 Å). The single Sb–Sb bond is 2.768 Å and is comparable to the double Sb covalent radius, 2.78 Å, but quite a bit shorter than the Sb–Sb interactions observed in

 $A_2 In_2 Sb_3$  (2.86–2.88 Å) or the  $[Sb@In_8 Sb_{12}]^{3-}$  and  $[Sb@In_8 Sb_{12}]^{5-}$  clusters (2.81–2.85 Å).

Superstructural ordering of clathrate materials is caused by either (i) ordering of the framework or guest vacancies 50-54 or (ii) preferences in the chemical bonding of the framework atoms with drastically different chemical nature.  $^{31,32,34,38,42,55,56}$  In the case of  $Cs_8In_{27}Sb_{19}$ , In and Sb distribution over the framework sites is coupled with a unit cell volume increase. This superstructure is a combination of klassengleich (k4) and translationengleich (t2) transformations.<sup>57</sup> For the unconventional transition metal clathrates, it has been shown that the nature of the observed clathrate ordering involves a preference in chemical bonding.<sup>38</sup> In the case of Ba-M-P (M = Ni, Cu, Zn, Au), site separation allows for the reduction or full elimination of M-M bonds within the framework. 30-32,34,36,37 Examination of the In-Sb framework in Cs<sub>8</sub>In<sub>27</sub>Sb<sub>19</sub> shows a similar trend, with the number of In-In and Sb-Sb bonds kept to a minimum while maximizing In-Sb interactions. Full elimination of In-In interactions, similar to the structure of binary InSb, is not possible as In contributes more than half of the atoms within the framework. Other clathrates, such as  $Cs_8Sn_{44}\square_2$  or  $Ba_8Ge_{43}\square_3$  (where  $\square$ denotes Sn or Ge vacancy in the framework), exhibit only klassengleich k4 transformation to the  $Ia\overline{3}d$  space group through an ordering of the framework vacancies.  $^{50-53}$  Cs<sub>8</sub>In<sub>27</sub>Sb<sub>19</sub> has an additional translationengleich t2 transformation that further splits framework sites, indicating that Cs<sub>8</sub>In<sub>27</sub>Sb<sub>19</sub> may need an additional type of ordering if certain interactions are to be reduced (e.g., In-In bonding). For instance, the splitting of the Pm3n 16i site eventually ends in discrete In and Sb sites in the  $Ia\overline{3}$  clathrate structure that would not be possible in either  $Pm\overline{3}n$  or  $Ia\overline{3}d$  structures (Figure 2A).

Two single-crystal X-ray diffraction solutions for the  $Cs_8In_{27}Sb_{19}$  structure are presented: one collected in-house at 100 K and the other synchrotron-based at 10 K. The two solutions match quite well, with only small thermally induced deviations in observed distances. Previous low temperature clathrate studies in  $Ae_8Ga_{16}Ge_{30}$  (Ae = Sr, Ba, Eu) showed that the guest position in the larger tetrakaidecahedron cage can split into many partially occupied positions around the cage.  $Se_{10} = Se_{10} =$ 

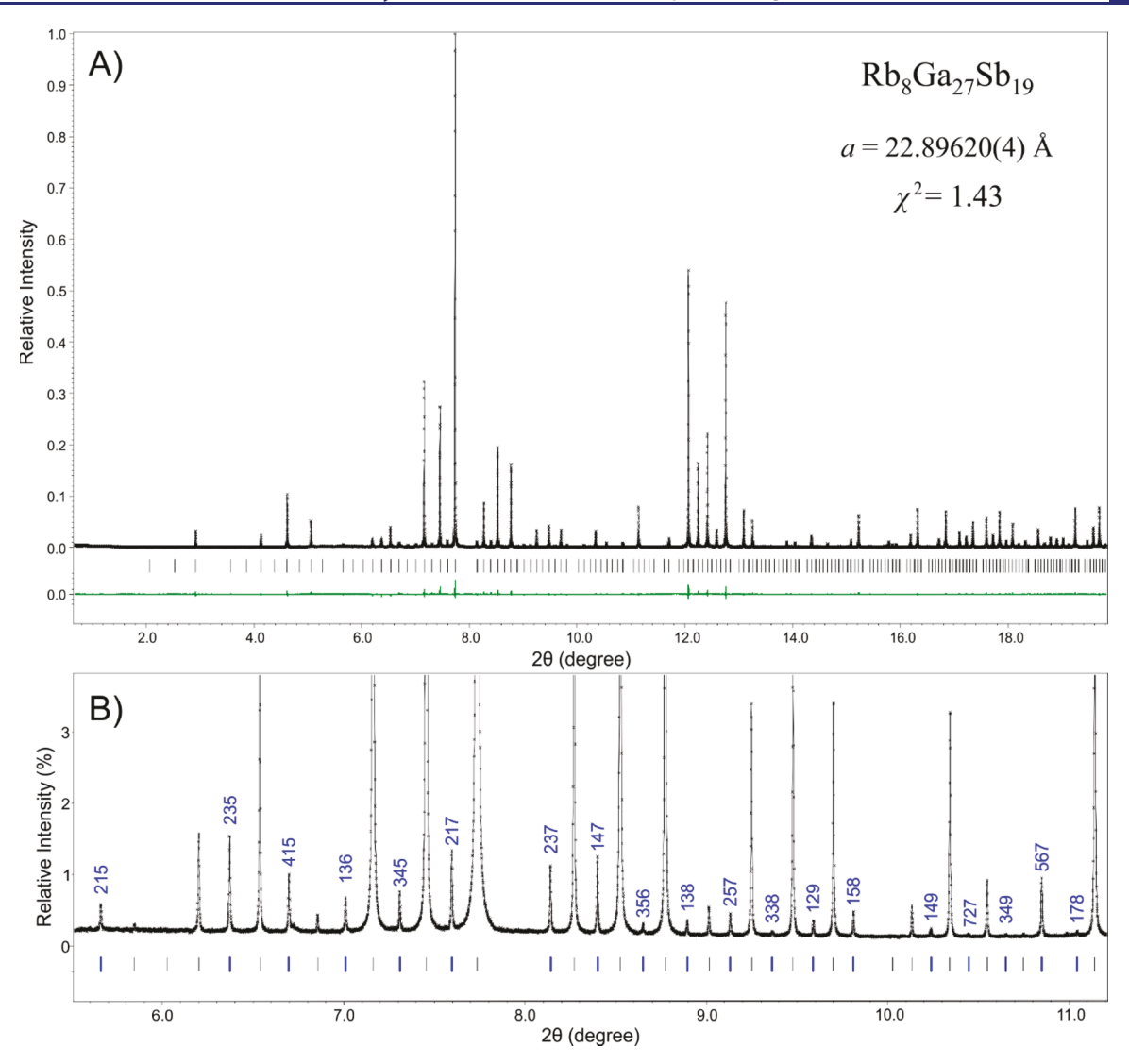


Figure 4. (A) PXRD pattern and corresponding Rietveld refinement (black line) of synchrotron powder X-ray diffraction data (black circles) for  $Rb_8Ga_{27}Sb_{19}$  collected at room temperature,  $\lambda=0.412\,75$  Å. Black ticks indicate the theoretical Bragg peak positions. The difference curve is shown in green at the bottom. (B) Fragment of the PXRD powder pattern with superstructural reflections tick marks and hkl indices highlighted in blue.

large cages, instead a flattening and expansion of the anisotropic parameters in the equatorial axis is shown.

Confirmation of the superstructure within bulk  $Cs_8In_{27}Sb_{19}$  samples was approached using high-resolution synchrotron PXRD. Small superstructural peaks are often hard to detect due to the low intensity caused by minute differences in Sb and In scattering factors. Peaks associated with the  $Ia\overline{3}$  superstructure were observed throughout the PXRD pattern for  $Cs_8In_{27}Sb_{19}$ , confirming that the superstructure is present throughout the bulk sample (Figure 3).

Crystal Structure of Rb<sub>8</sub>Ga<sub>27</sub>Sb<sub>19</sub> and Cs<sub>8</sub>Ga<sub>27</sub>Sb<sub>19</sub>. The crystal structures of the Ga analogues were difficult to establish using single-crystal diffraction due to heavy twinning of the studied crystals. For Cs<sub>8</sub>Ga<sub>27</sub>Sb<sub>19</sub>, the reported model was achieved using in-house single crystal data with atomic displacement parameters for two framework sites fixed and not refined (Table S4). This model was validated by the refinement of synchrotron PXRD data. For Rb<sub>8</sub>Ga<sub>27</sub>Sb<sub>19</sub>, no suitable crystals were found, and the crystal structure was established by means of Rietveld refinement of synchrotron PXRD data (Figure 4). The crystal structure of Cs<sub>8</sub>In<sub>27</sub>Sb<sub>19</sub>

was used to generate the initial model. Final structural refinement corroborates that  $Rb_8Ga_{27}Sb_{19}$  is isostructural to  $Cs_8In_{27}Sb_{19}$  with the same superstructural ordering,  $2a \times 2a \times 2a$  in the cubic  $Ia\overline{3}$  space group. The intensity of the superstructural reflections is proportional to the difference in scattering factors of metal (Ga or In) and antimony. This is the reason why the superstructural reflections are extremely weak (<0.15%) for  $Cs_8In_{27}Sb_{19}$  (Figure 3). Due to the higher X-ray scattering contrast of Ga and Sb (atomic numbers 31 and 51), the reflections corresponding to the superstructural ordering are more intense in the case of  $Rb_8Ga_{27}Sb_{19}$  (Figure 4B). Additional refinement details and atomic coordinates for  $Cs_8Ga_{27}Sb_{19}$  and  $Rb_8Ga_{27}Sb_{19}$  can be found in Tables S1, S4, and S5.

 $Rb_8Ga_{27}Sb_{19}$  and  $Cs_8Ga_{27}Sb_{19}$  are isostructural to  $Cs_8In_{27}Sb_{19}$ , crystallizing in the  $\emph{Ia}\overline{3}$  superstructure. Atomic segregation of Ga and Sb on the clathrate framework is obvious due to their distinct X-ray scattering coefficients. The Ga–Sb interactions in  $Rb_8Ga_{27}Sb_{19}$  (2.649(1)–2.726(2) Å) and  $Cs_8Ga_{27}Sb_{19}$  (2.623(2)–2.751(2) Å) are slightly longer than those reported for  $Rb_2GaSb_2$  (2.555–2.644 Å),  $^{62}$   $Cs_2GaSb_2$ 

(2.550–2.599 Å), $^{63}$  and  $Cs_6GaSb_3$  (2.608–2.676 Å). $^{64}$  The Ga–Ga bond distances in  $Rb_8Ga_{27}Sb_{19}$  and  $Cs_8Ga_{27}Sb_{19}$  are similar, 2.471(2)–2.561(3) Å, which are longer than double covalent radius of Ga, 2.44 Å, which are longer than double covalent radius of Ga, 2.44 Å, which are longer than double covalent radius of  $Cs_8Ga_{27}Sb_{19}$  and  $Cs_8Ga_{27}Sb_{19}$  are 2.709(1) and 2.745(3) Å, respectively. These distances are frequently observed in ternary antimonides such as  $EuFe_4Sb_{12}$  (2.749 Å), $^{66}$   $Ce_{12}Ge_{5.2}Sb_{26.8}$  (2.619–2.797 Å), $^{67}$  and  $Eu_{11}Zn_6Sb_{12}$  (2.795 Å). $^{68}$ 

Synthesis and Thermal Stability. The synthesis of Cs<sub>8</sub>In<sub>27</sub>Sb<sub>19</sub> can be achieved by a stoichiometric reaction of the elements or through the use of binary precursors. All reactions must be performed within welded Ta ampules to offset the high vapor pressure of Cs at elevated temperatures. Homogenization of the samples made from elements is not fully achievable, even when applying multiple grinding and reannealing cycles, as admixtures of ductile In metal tend to segregate. To remedy this problem, a mixture of Cs and In metals and InSb in a ratio of 8:8:19 was used to improve the initial mixing and reactivity, reducing the amount of metallic In initially within the sample. The result was a nearly phase-pure sample of Cs<sub>8</sub>In<sub>27</sub>Sb<sub>19</sub>, with only a small admixture of InSb present after three annealing cycles (Figure S1). Annealing temperatures higher than 823 K lead to formation of Cs<sub>2</sub>In<sub>2</sub>Sb<sub>3</sub> and Ta<sub>3</sub>Sb admixtures.

In the case of  $A_8Ga_{27}Sb_{19}$  (A = Rb, Cs) there was no detectable difference in the synthesis using stoichiometric reaction of the elements or via the aid of presynthesized binary GaSb precursors. The synthesis process of  $A_8$ Ga<sub>27</sub>Sb<sub>19</sub> (A =Rb, Cs) samples were optimized using DSC data (Figure S2), indicating higher thermal stability for Cs<sub>8</sub>Ga<sub>27</sub>Sb<sub>19</sub>, which decomposes around 1001(3) K, while Rb<sub>8</sub>Ga<sub>27</sub>Sb<sub>19</sub> can only sustain heating up to 975(3) K. The final syntheses of Cs<sub>8</sub>Ga<sub>27</sub>Sb<sub>19</sub> and Rb<sub>8</sub>Ga<sub>27</sub>Sb<sub>19</sub> were carried out at 973 and 943 K, respectively. After three annealings, gray uniform powder of Rb<sub>8</sub>Ga<sub>27</sub>Sb<sub>19</sub> was collected without the presence of detectable Ga admixtures (Figure 4). Single-phase samples can be alternatively synthesized using a GaSb precursor. The Cs<sub>8</sub>Ga<sub>27</sub>Sb<sub>19</sub> compound has not been synthesized as a singlephase sample according to PXRD, but samples where Cs<sub>8</sub>Ga<sub>27</sub>Sb<sub>19</sub> was the main product were produced (Figure S3).

The as-synthesized samples of Cs<sub>8</sub>In<sub>27</sub>Sb<sub>19</sub> do not initially appear to be air-sensitive, with no noticeable change in their PXRD within a few hours of air exposure. Nevertheless, SEM analyses reveals oxide formation on the surface of the material when only briefly exposed to ambient conditions. SEM performed in anaerobic conditions using an air-sensitive holder reveals no presence of oxides, indicating the oxides formed during brief air exposure. Submersion of Cs<sub>8</sub>In<sub>27</sub>Sb<sub>19</sub> in water results in gas release and decomposition. Both A<sub>8</sub>Ga<sub>27</sub>Sb<sub>19</sub> samples were more sensitive to ambient conditions, with PXRD showing decomposition after 2 h of air exposure. Because of the relatively high humidity levels at ambient conditions, currently it is not clear whether the III–V clathrates are sensitive to air, humidity, or both.

Differential scanning calorimetry (DSC) was used to elucidate the thermal stability of  $Cs_8In_{27}Sb_{19}$  (Figures 5 and S4). Three endothermic peaks are visible in the heating curve, at 423, 850, and 943 K. The measured sample had a small admixture of In, which correlates well to the first peak ( $T_{\rm melt}(In) = 430$  K). The next two peaks were assessed using *in situ* synchrotron PXRD studies on a sample containing  $Cs_8In_{27}Sb_{19}$  and admixtures of InSb and In (Figure 6). The

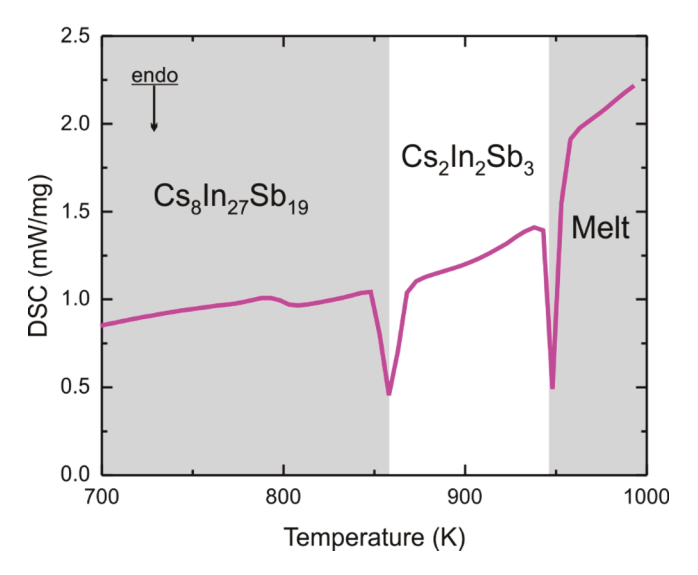


**Figure 5.** DSC heating curve for  $Cs_8In_{27}Sb_{19}$ . The stability regions for different phases are highlighted.

InSb and In peaks begin to disappear at lower temperatures as expected, though InSb is slightly below its reported melting point of 799 K. Peaks assigned to  $Cs_8In_{27}Sb_{19}$  do not change until past 800 K, when they begin to change into peaks associated with  $Cs_2In_2Sb_3$ . <sup>69</sup> The full conversion is finished by 840 K. The melting of  $Cs_2In_2Sb_3$  occurs at 952 K (data not shown). These data allow us to assign the first peak in Figure 5 to the decomposition of  $Cs_8In_{27}Sb_{19}$  and the second one to melting of  $Cs_3In_2Sb_3$ .

 $Cs_8Ga_{27}Sb_{19}$  exhibits one exothermic peak upon heating and a single endothermic peak during cooling, which corresponds to thermal decomposition (Figure S2) as evidenced by PXRD (Figure S5). Rb $_8Ga_{27}Sb_{19}$  thermal behavior is similar to that of  $Cs_8In_{27}Sb_{19}$  (Figure S2), with two exothermic peaks at 961 and 975 K during the heating process, while only one endothermic peak was present upon cooling. After the DSC experiment, the sample of  $Rb_8Ga_{27}Sb_{19}$  was found to degrade into GaSb and a few unidentified peaks in the PXRD (Figure S5). Unlike the  $Cs_8In_{27}Sb_{19}$  clathrate, the two exothermic peaks of  $Rb_8Ga_{27}Sb_{19}$  are very close to each other, less than 15 K apart; thus it is challenging to extract phase information within this small interval.

**Density Functional Theory.** The equilibrium lattice parameters, the formation energy, and the bulk modulus of novel III–V clathrates were computed by fitting the total energy as a function of volume on the Vinet equation of state. The theoretical lattice parameters are in good agreement (1.7–2.6% larger) with those determined by X-ray diffraction (Table S7).  $Cs_8In_{27}Sb_{19}$  is softer than the Gacontaining clathrates, which feature ~25% larger bulk modulus. In the latter compounds, switching of the cation does not significantly affect either lattice parameter or bulk modulus.

Stability of III–V clathrates was probed by computing their energy with respect to the Hull curve, *i.e.* the energy of decomposition into the set of most stable materials for the given composition in the ternary phase diagram. According to the ternary phase diagram in Figure 7A, Cs<sub>8</sub>In<sub>27</sub>Sb<sub>19</sub> decomposes into In, InSb, and Cs<sub>2</sub>In<sub>2</sub>Sb<sub>3</sub>, agreeing well with experimental results. Computing the equation of states and total energy for all compounds in which clathrate would decompose shows that at zero temperature the energy of

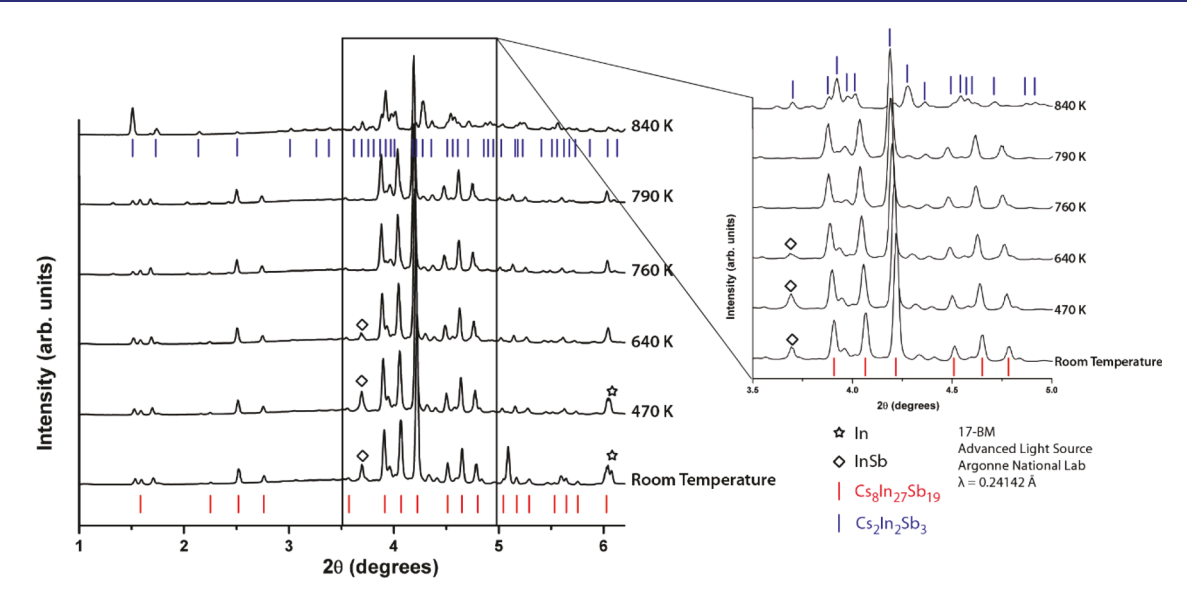


Figure 6. In situ variable temperature synchrotron PXRD of  $Cs_8In_{27}Sb_{19}$  sample, with a zoomed selected  $2\theta$  region shown ( $\lambda = 0.24142$  Å). Admixtures of InSb and In are denoted by diamonds and stars, respectively. The sample was heated from room temperature (bottom pattern) to 840 K (top pattern). Calculated peak positions for  $Cs_8In_{27}Sb_{19}$  and  $Cs_2In_2Sb_3$  and are shown as red and blue thick lines, respectively.

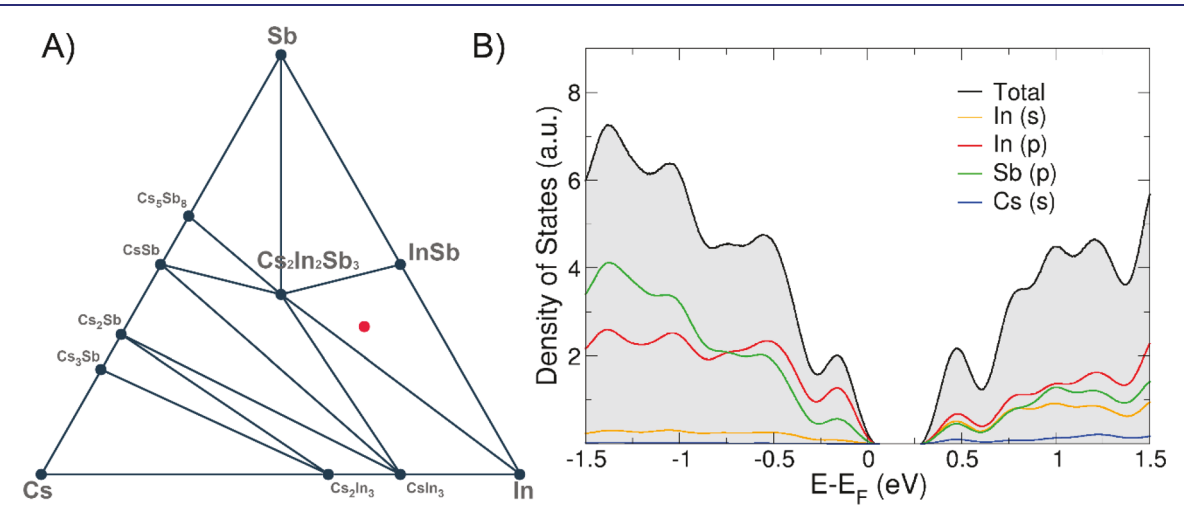


Figure 7. (A) Ternary phase diagram for the Cs–In–Sb system. The composition for  $Cs_8In_{27}Sb_{19}$  is indicated by the solid red dot. (B) Calculated density of states for  $Cs_8In_{27}Sb_{19}$ .

 $Cs_8In_{27}Sb_{19}$  is 0.036 eV/atom below the Hull, indicating that the compound is stable at low temperature. The Ga-containing analogues are also stable against decomposition by 0.053 eV/atom (Cs–Ga) and 0.060 eV/atom (Rb–Ga).

 $Cs_8In_{27}Sb_{19}$  (like  $Cs_8Ga_{27}Sb_{19}$  and  $Rb_8Ga_{27}Sb_{19}$ ) is an electron precise compound and thus a semiconductor. Its parent phase, InSb, is a direct band-gap semiconductor with a narrow gap of 0.24 eV (experimental).<sup>71</sup> In DFT calculations, InSb appears semimetallic, with a vanishing gap at the  $\Gamma$ -point. This is a well-known shortcoming of DFT, which tends to systematically underestimate band gaps of III–V semiconductors with a mean relative error of ~40%.<sup>72</sup> Our DFT calculations predict that  $Cs_8In_{27}Sb_{19}$  is a semiconductor with a 0.34 eV indirect band gap. Notably, the direct transition at the H-point is close in value at 0.41 eV (Figure S11). A small density of Cs vacancies would make the material a p-type semiconductor and may be the origin of the positive Seebeck coefficient observed in the transport measurements (*vide infra*). The valence band density of states (DOS) of

 $Cs_8In_{27}Sb_{19}$  (Figure 7B) is significantly steeper than that of InSb, leading to a high Seebeck coefficient as shown in experiments. Besides this marked difference, the DOS projected on the atomic wave function of the clathrate has a similar character to that of its parent InSb phase; i.e., the valence band is contributed by In- and Sb-5p states in  $\sim$ 2:1 ratio, while the conduction band is made of In-5s and -5p and Sb-5p states in almost equal amounts. The contribution of Cs states is negligible, indicating that Cs guest atoms completely donate their s electron to the clathrate structure. The curvature of the valence bands at the *H*-point is sufficient to provide small hole effective mass and thus high mobility (Figure S11). A full set of ternary phase diagrams, DOS, and tables of calculated parameters can be found in the Supporting Information (Figures S5–S13 and Table S7).

**Transport Properties.** Electronic and thermal transport measurements were performed on pelletized samples of the novel clathrates in the temperature regime of 10–300 K (Figure 8). All three compounds exhibit a typical dependence

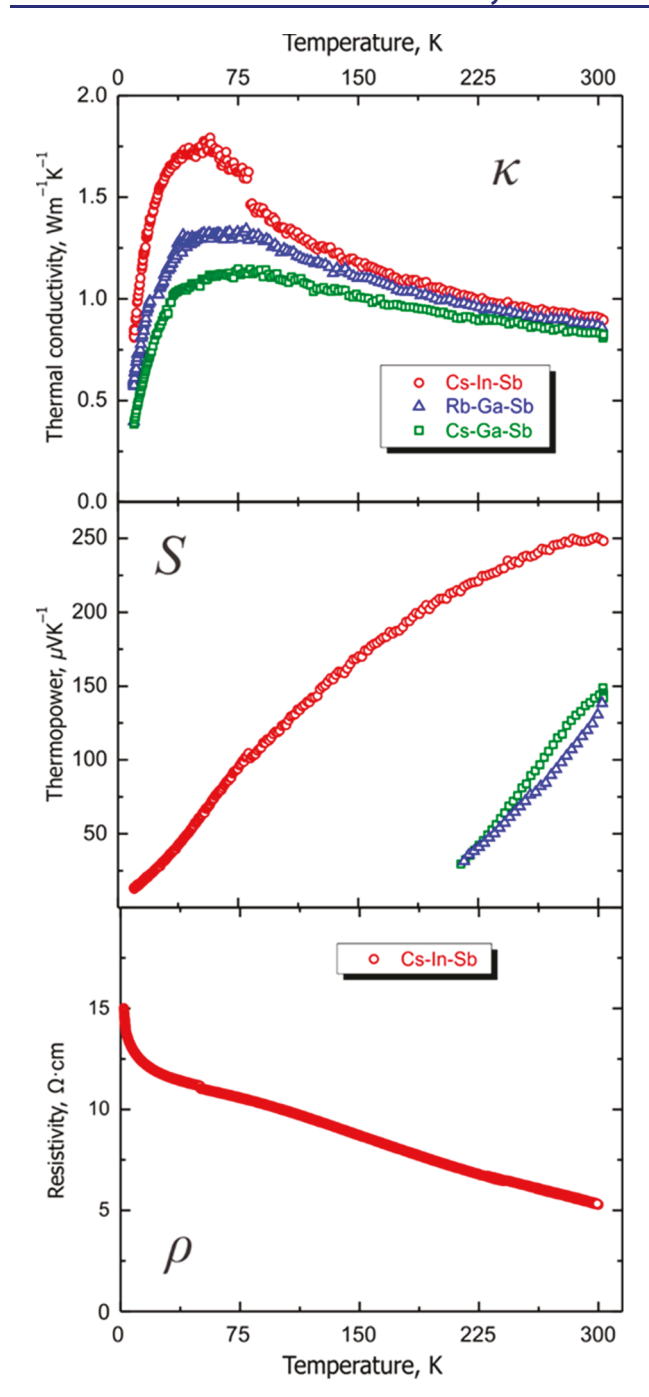


**Figure 8.** Transport properties of III–V clathrates: (top) thermal conductivity, (middle) Seebeck coefficient, and (bottom) electrical resistivity.  $Cs_8In_{27}Sb_{19}$ : red circles.  $Cs_8Ga_{27}Sb_{19}$ : green squares.  $Rb_8Ga_{27}Sb_{19}$ : blue triangles.

of the thermal conductivity for crystalline materials with a maximum around 50 K. For several Sn-based clathrates, glass-like behavior of the thermal conductivity was reported, which lacks this maximum at low temperature. This behavior was associated with the displacement of guest cations from the center of larger tetrakaidecahedral cages.  $^{73,74}$  Our 10 K single crystal diffraction experiment for  $\rm Cs_8 In_{27}Sb_{19}$  exhibits no such displacement of Cs atoms, in accordance with the observed peak in the thermal conductivity at 50 K.

At room temperature, the thermal conductivity for all three compounds is comparable, 0.8–0.9 W·m<sup>-1</sup>·K<sup>-1</sup> (Figure 8).

While low thermal conductivities of  $1-3~W\cdot m^{-1}\cdot K^{-1}$  are typical for conventional and transition metal clathrates,  $^{38,42,75}$  values below  $1~W\cdot m^{-1}\cdot K^{-1}$  were achieved only for clathrates containing heavy elements (Sn or Au) in the framework, such as  $Ba_8Au_{16}P_{30}$  or  $Ba_8Ga_{16}Sn_{30}$  with thermal conductivities below  $0.7~W\cdot m^{-1}\cdot K^{-1}$  at room temperature. Large superstructural unit cells and the presence of heavy atoms in the framework are likely responsible for such ultralow values of the thermal conductivity. The electronic and lattice contributions to the thermal conductivity were extracted, showing a majority of the contribution coming from lattice transport (>99.9%).

Cs<sub>8</sub>In<sub>27</sub>Sb<sub>19</sub> exhibits p-type semiconducting behavior, with large positive Seebeck thermopower values of 250  $\mu$ V·K<sup>-1</sup> at 300 K (Figure 8). High Seebeck values and the ordered framework superstructure indicate that Cs<sub>8</sub>In<sub>27</sub>Sb<sub>19</sub> is an electron precise compound, in good agreement with the calculated band structure. The curvature of the Seebeck curve appears as though it may be reaching a maximum near room temperature, before decreasing due to the bipolar effect (excitation of electrons into the conduction band), although the high-temperature measurements have not been performed to prove this. If the maximum is taken to occur at 300 K, a Goldsmid-Sharp band-gap estimation of  $E_{\rm g} = 2e|S_{\rm max}|T_{\rm max} =$ 0.15 eV indicates a narrow-band gap for Cs<sub>8</sub>In<sub>27</sub>Sb<sub>19</sub>, <sup>79</sup> which is similar to the calculated band gap of 0.34 eV, taking into account accuracy of the band-gap prediction by DFT. Seebeck coefficients for the Ga-clathrates are lower, reaching 150 µV· K<sup>-1</sup> at 300 K (Figure 8). Due to the high resistivity of Gacontaining compounds, the thermopower could only be measured in a limited temperature range. High values of the thermopower are not uncharted, with some tetrel-based p-type clathrates having shown similar values at room temperature  $\begin{array}{l} (Ba_8Au_{5.3}Ge_{40.7},\,348~\mu\mathrm{V\cdot K^{-1}};\,Ba_8Ga_{16}Zn_{3.2}Ge_{26.8},\,250~\mu\mathrm{V\cdot K^{-1}};\\ Ba_8Ga_{16}Sn_{30},\,150-370~\mu\mathrm{V\cdot K^{-1}}).^{77,78,80,81} \end{array}$ 

Electrical resistivity of  $Cs_8In_{27}Sb_{19}$  decreases with temperature but did not show an exponential temperature dependence typical for conventional semiconductors. Resistivity almost linearly decreases in the 50–300 K range indicating heavily doped semiconducting behavior in line with the small band gap detected from thermopower measurements and computations (Figure 8). The room temperature resistivity value for  $Cs_8In_{27}Sb_{19}$  of 5.3  $\Omega$ ·cm is slightly higher than that for other ternary triel-antimonides (KGaSb<sub>2</sub>, 2.0  $\Omega$ ·cm;  $Ca_3AlSb_3$ , 1.5  $\Omega$ ·cm;  $Sr_3GaSb_3$ , 0.5  $\Omega$ ·cm;  $Cs_5Al_2Sb_6$ , 0.4  $\Omega$ ·cm).  $S^2-S^2$  No reliable electrical resistivity measurements were achieved for Ga-containing clathrate samples, presumably due to the high air-sensitivity of the samples resulting in surface oxidation.

The most intriguing property of these novel clathrates is hole mobility. As mentioned in the Introduction, for tetrel-based clathrates low mobilities have been reported, typically well below 50 cm² V $^{-1}$  s $^{-1}$  and one exceptional case of 170 cm² V $^{-1}$  s $^{-1.25}$  By use of Hall measurements, the hole mobilities and concentrations were established for Cs<sub>8</sub>In<sub>27</sub>Sb<sub>19</sub>. Binary InSb has a high hole carrier mobility of ~800 cm² ·V $^{-1}$ ·s $^{-1}$  and room temperature hole concentrations ranging from ~10<sup>15</sup> to  $10^{16}$  cm $^{-3.87,88}$  The complex clathrate Cs<sub>8</sub>In<sub>27</sub>Sb<sub>19</sub> inherits such properties with similar mobility and concentration values, 880 cm² ·V $^{-1}$ ·s $^{-1}$  and 1.42 × 10<sup>15</sup> cm $^{-3}$ . This is dissimilar to other reports of p-type ternary compounds containing III–V fragments, such as in the supertetrahedral layered compounds Ae<sub>15</sub>Tr<sub>22</sub>As<sub>32</sub> and Ae<sub>3</sub>Ga<sub>6</sub>As<sub>8</sub> (Ae = Sr, Eu; Tr = Ga, In), in

which there is a substantial decrease in mobility down to 0.2–98 cm $^2 \cdot V^{-1} \cdot s^{-1}$  going from the binary to ternary compounds. High hole mobility within bulk samples at room temperature is uncommon but can still be found in some compounds, such as doped  $CsBi_4Te_6~(700-1000~cm^2 \cdot V^{-1} \cdot s^{-1}),~CoP_3~(748~cm^2 \cdot V^{-1} \cdot s^{-1}),~or~CoSb_3~(1500-2970~cm^2 \cdot V^{-1} \cdot s^{-1}).^{90-92}$  The ordered nature of the In–Sb framework may be a key to the high mobility of  $Cs_8In_{27}Sb_{19}.$  It was shown that defects may significantly affect the electronic and optical properties of III–V semiconductors.

Obtaining high mobility in clathrates has enormous potential because of their tunability. In binary III-V semiconductors, aliovalent doping is used to modify carrier concentration and band structure to affect the electronic properties. Such doping is limited to a ppm concentration level of dopants. In the case of clathrates, aliovalent substitution was shown to be effective not only in adjusting the carrier concentration and type but also in inducing metal-to-semiconductor transitions. For example, Ba<sub>8</sub>Cu<sub>16</sub>P<sub>30</sub> clathrate exhibited multiple metal-tosemiconductor transitions upon replacement of the part of Cu atoms with Zn. 34,35,37 Thus, aliovalent substitution in III-V clathrates opens ways to designing materials with high mobility and tunable carrier concentrations, which is desirable for optoelectronic and thermoelectric applications. The stability of the III-V clathrate can be improved by introducing stronger covalent bonds in the framework, for example, by increasing the electronegativity difference between group 13 metal and pnictide. In-Sb and Ga-Sb based clathrates reported here open a window of possibilities for designing functional materials based on clathrates with intrinsically high mobility. Moreover, this discovery indicates that other binary semiconductors, for example, II-VI, can be converted into clathrates using proper design principles.

## CONCLUSION

The first examples of fully main group tetrel-free unconventional clathrates, Cs<sub>8</sub>In<sub>27</sub>Sb<sub>19</sub>, Cs<sub>8</sub>Ga<sub>27</sub>Sb<sub>19</sub>, and Rb<sub>8</sub>Ga<sub>27</sub>Sb<sub>19</sub>, are presented. These clathrates crystallize in a Ia3 superstructure of the type-I clathrate, with the framework elements segregating into individual sites. A combination of highresolution synchrotron powder and single-crystal X-ray diffraction was utilized to elucidate the structures. Highresolution PXRD indicates that the structural ordering is present throughout the bulk sample. DFT calculations show that all clathrates are energetically stable semiconductors with bandgaps ranging from 0.34 to 0.81 eV. Basic thermal and charge transport properties were characterized for Cs<sub>8</sub>In<sub>27</sub>Sb<sub>19</sub>, Cs<sub>8</sub>Ga<sub>27</sub>Sb<sub>19</sub>, and Rb<sub>8</sub>Ga<sub>27</sub>Sb<sub>19</sub>, showing low thermal conductivity, ranging between 0.8 and 0.9 W·m<sup>-1</sup>·K<sup>-1</sup> at room temperature. The clathrates exhibit p-type semiconducting behavior, with high thermopower values of 250  $\mu$ V·K<sup>-1</sup> (In) and 150  $\mu$ V·K<sup>-1</sup> (Ga) at 300 K. Hall measurements for  $Cs_8In_{27}Sb_{19}$  show a carrier concentration of 1.4  $\times$  10<sup>15</sup> cm<sup>-3</sup> and extraordinary hole mobility of 880 cm<sup>2</sup> ·V<sup>-1</sup>·s<sup>-1</sup> at 300 K. The mobility of the novel Cs<sub>8</sub>In<sub>27</sub>Sb<sub>19</sub> clathrate is on par with those for one of the best binary semiconductors, InSb, making the discovery of III-V clathrates quite intriguing as many III-V binary semiconductors have been studied and used in highprofile electronic applications. High tolerance of unconventional clathrates to aliovalent substitutions allows for tuning of carrier concentration in a wide range, which is a desirable property for high mobility semiconductors. Whether other types of simple binary semiconductors, i.e., II-VI, can be converted into clathrates is currently under investigation.

#### ASSOCIATED CONTENT

# **5** Supporting Information

The Supporting Information is available free of charge at https://pubs.acs.org/doi/10.1021/jacs.9b12351.

Experimental details, figures, and tables pertinent to characterization techniques used: powder and single crystal X-ray diffraction, energy dispersive X-ray spectroscopy, differential scanning calorimetry, spark plasma sintering, transport property measurements, electronic structure calculations, bands and DOS diagrams, and calculated ternary phase diagrams (PDF)

Crystallographic information (CIF)

Crystallographic information (CIF)

Crystallographic information (CIF)

Crystallographic information (CIF)

#### AUTHOR INFORMATION

#### **Corresponding Author**

Kirill Kovnir — Iowa State University, Ames, Iowa, and U.S. Department of Energy, Ames, Iowa; orcid.org/0000-0003-1152-1912; Email: kovnir@iastate.edu

#### Other Authors

Bryan Owens-Baird — Iowa State University, Ames, Iowa, and U.S. Department of Energy, Ames, Iowa; orcid.org/0000-0003-3128-5363

Jian Wang — Iowa State University, Ames, Iowa, U.S. Department of Energy, Ames, Iowa, and Wichita State University, Wichita, Kansas; ⊙ orcid.org/0000-0003-1326-4470

Suyin Grass Wang – The University of Chicago, Lemont, Illinois

**Yu-Sheng Chen** – The University of Chicago, Lemont, Illinois

Shannon Lee — Iowa State University, Ames, Iowa, and U.S. Department of Energy, Ames, Iowa; ⊚ orcid.org/ 0000-0002-7541-3286

**Davide Donadio** − *University of California, Davis, Davis, California;* o orcid.org/0000-0002-2150-4182

Complete contact information is available at: https://pubs.acs.org/10.1021/jacs.9b12351

## **Author Contributions**

<sup>#</sup>B.O.-B. and J.W. equally contributed to the work.

#### Notes

The authors declare no competing financial interest.

## ACKNOWLEDGMENTS

The authors are thankful to Dr. S. Lapidus, Dr. W. Xu, and Dr. A. Yakovenko (APS ANL) for collecting high-resolution and *in situ* synchrotron XRD patterns and to Prof. J. Zaikina (ISU) for access to the SPS and arc-welder. This research was supported by the U.S. Department of Energy, Office of Basic Energy Sciences, Division of Materials Science and Engineering under Award DE-SC0008931. NSF's ChemMatCARS Sector 15 is supported by the Divisions of Chemistry (CHE) and Materials Research (DMR), National Science Foundation, under Grant

NSF/CHE-1834750. Use of the Advanced Photon Source, an Office of Science User Facility operated for the U.S. Department of Energy (DOE) Office of Science by Argonne National Laboratory, was supported by the U.S. DOE under Contract DE-AC02-06CH11357.

#### REFERENCES

- (1) Kohl, P. A.; Bard, A. J. Semiconductor electrodes. 13. Characterization and behavior of n-type zinc oxide, cadmium sulfide, and gallium phosphide electrodes in acetonitrile solutions. *J. Am. Chem. Soc.* 1977, 99 (23), 7531–7539.
- (2) Beberwyck, B. J.; Alivisatos, A. P. Ion Exchange Synthesis of III—V Nanocrystals. J. Am. Chem. Soc. 2012, 134 (49), 19977–19980.
- (3) Harris, D. K.; Bawendi, M. G. Improved Precursor Chemistry for the Synthesis of III–V Quantum Dots. *J. Am. Chem. Soc.* **2012**, *134* (50), 20211–20213.
- (4) Liu, W.; Chang, A. Y.; Schaller, R. D.; Talapin, D. V. Colloidal InSb Nanocrystals. J. Am. Chem. Soc. 2012, 134 (50), 20258–20261.
- (5) Srivastava, V.; Liu, W.; Janke, E. M.; Kamysbayev, V.; Filatov, A. S.; Sun, C.-J.; Lee, B.; Rajh, T.; Schaller, R. D.; Talapin, D. V. Understanding and Curing Structural Defects in Colloidal GaAs Nanocrystals. *Nano Lett.* **2017**, *17* (3), 2094–2101.
- (6) Nainani, A.; Bennett, B. R.; Boos, J. B.; Ancona, M. G.; Saraswat, K. C. Enhancing hole mobility in III-V semiconductors. *J. Appl. Phys.* **2012**, *111* (10), 103706.
- (7) Jacoboni, C.; Canali, C.; Ottaviani, G.; Alberigi Quaranta, A. A review of some charge transport properties of silicon. *Solid-State Electron.* **1977**, 20 (2), 77–89.
- (8) Prince, M. B. Drift Mobilities in Semiconductors. II. Silicon. *Phys. Rev.* **1954**, 93 (6), 1204–1206.
- (9) Golikova, O. A.; Moizhez, B. Y.; Stilbans, L. S. Hole mobility of germanium as a function of concentration and temperature. *Sov. Phys. Solid State* **1962**, *3*, 2259–2265.
- (10) Prince, M. B. Drift Mobilities in Semiconductors. I. Germanium. *Phys. Rev.* **1953**, 92 (3), 681–687.
- (11) Germanium (Ge), hole mobility. In *Group IV Elements, IV-IV* and *III-V Compounds. Part b Electronic, Transport, Optical and Other Properties*; Madelung, O., Rössler, U., Schulz, M., Eds.; Springer: Berlin, 2002; pp 1–13.
- (12) Wallentin, J.; Anttu, N.; Asoli, D.; Huffman, M.; Åberg, I.; Magnusson, M. H.; Siefer, G.; Fuss-Kailuweit, P.; Dimroth, F.; Witzigmann, B.; Xu, H. Q.; Samuelson, L.; Deppert, K.; Borgström, M. T. InP Nanowire Array Solar Cells Achieving 13.8% Efficiency by Exceeding the Ray Optics Limit. *Science* 2013, 339 (6123), 1057–1060.
- (13) del Alamo, J. A. Nanometre-scale electronics with III–V compound semiconductors. *Nature* **2011**, 479 (7373), 317–323.
- (14) Cariou, R.; Benick, J.; Feldmann, F.; Höhn, O.; Hauser, H.; Beutel, P.; Razek, N.; Wimplinger, M.; Bläsi, B.; Lackner, D.; Hermle, M.; Siefer, G.; Glunz, S. W.; Bett, A. W.; Dimroth, F. III–V-on-silicon solar cells reaching 33% photoconversion efficiency in two-terminal configuration. *Nat. Energy* **2018**, 3 (4), 326–333.
- (15) Yoon, J.; Jo, S.; Chun, I. S.; Jung, I.; Kim, H.-S.; Meitl, M.; Menard, E.; Li, X.; Coleman, J. J.; Paik, U.; Rogers, J. A. GaAs photovoltaics and optoelectronics using releasable multilayer epitaxial assemblies. *Nature* **2010**, *465*, 329.
- (16) Chen, S.; Li, W.; Wu, J.; Jiang, Q.; Tang, M.; Shutts, S.; Elliott, S. N.; Sobiesierski, A.; Seeds, A. J.; Ross, I.; Smowton, P. M.; Liu, H. Electrically pumped continuous-wave III—V quantum dot lasers on silicon. *Nat. Photonics* **2016**, *10*, 307.
- (17) Dietrich, C. P.; Fiore, A.; Thompson, M. G.; Kamp, M.; Höfling, S. GaAs integrated quantum photonics: Towards compact and multi-functional quantum photonic integrated circuits. *Laser Photonics Rev.* **2016**, *10* (6), 870–894.
- (18) Guloy, A. M.; Ramlau, R.; Tang, Z.; Schnelle, W.; Baitinger, M.; Grin, Y. A guest-free germanium clathrate. *Nature* **2006**, 443 (7109), 320–323.

- (19) Ammar, A.; Cros, C.; Pouchard, M.; Jaussaud, N.; Bassat, J.-M.; Villeneuve, G.; Duttine, M.; Ménétrier, M.; Reny, E. On the clathrate form of elemental silicon, Si<sub>136</sub>: preparation and characterisation of Na<sub>x</sub>Si<sub>136</sub> (x→0). *Solid State Sci.* **2004**, *6* (5), 393–400.
- (20) Bryan, J. D.; Blake, N. P.; Metiu, H.; Stucky, G. D.; Iversen, B. B.; Poulsen, R. D.; Bentien, A. Nonstoichiometry and chemical purity effects in thermoelectric Ba<sub>8</sub>Ga<sub>16</sub>Ge<sub>30</sub> clathrate. *J. Appl. Phys.* **2002**, 92 (12), 7281–7290.
- (21) Anno, H.; Hokazono, M.; Shirataki, R.; Nagami, Y. Crystallographic, thermoelectric, and mechanical properties of polycrystalline type-I Ba<sub>8</sub>Al<sub>16</sub>Si<sub>30</sub>-based clathrates. *J. Mater. Sci.* **2013**, *48* (7), 2846–2854.
- (22) Yan, X.; Ikeda, M.; Zhang, L.; Bauer, E.; Rogl, P.; Giester, G.; Prokofiev, A.; Paschen, S. Suppression of vacancies boosts thermoelectric performance in type-I clathrates. *J. Mater. Chem. A* **2018**, 6 (4), 1727–1735.
- (23) He, Y.; Sui, F.; Kauzlarich, S. M.; Galli, G. Si-based Earth abundant clathrates for solar energy conversion. *Energy Environ. Sci.* **2014**, 7 (8), 2598–2602.
- (24) Kishimoto, K.; Akai, K. Thermoelectric and transport properties of sintered type-II clathrate Cs<sub>8</sub>Ba<sub>16</sub>Ga<sub>40</sub>Sn<sub>96</sub>. *Jpn. J. Appl. Phys.* **2019**, 58 (10), 101002.
- (25) Kishimoto, K.; Koda, S.; Akai, K.; Koyanagi, T. Thermoelectric properties of sintered type-II clathrates (K, Ba)<sub>24</sub>(Ga, Sn)<sub>136</sub> with various carrier concentrations. *J. Appl. Phys.* **2015**, *118* (12), 125103.
- (26) Eisenmann, B.; Schäfer, H.; Zagler, R. Die verbindungen  $A^{II}_{8}B^{III_{16}}B^{IV_{30}}$  ( $A^{II} \equiv Sr$ , Ba;  $B^{III} \equiv Al$ , Ga;  $B^{IV} \equiv Si$ , Ge, Sn) und ihre käfigstrukturen. J. Less-Common Met. 1986, 118 (1), 43–55.
- (27) Sui, F.; He, H.; Bobev, S.; Zhao, J.; Osterloh, F. E.; Kauzlarich, S. M. Synthesis, Structure, Thermoelectric Properties, and Band Gaps of Alkali Metal Containing Type I Clathrates:  $A_8Ga_8Si_{38}$  (A = K, Rb, Cs) and  $K_8Al_8Si_{38}$ . Chem. Mater. **2015**, 27 (8), 2812–2820.
- (28) Xu, J.; Wu, J.; Heguri, S.; Tanabe, Y.; Liu, G.-Q.; Jiang, J.; Jiang, H.; Tanigaki, K. Single Crystal Structure Study of Type I Clathrate  $K_8Zn_4Sn_{42}$  and  $K_8In_8Sn_{38}$ . J. Electron. Mater. **2017**, 46 (5), 2765–2769
- (29) Mudryk, Y.; Rogl, P.; Paul, C.; Berger, S.; Bauer, E.; Hilscher, G.; Godart, C.; No l, H. Thermoelectricity of clathrate I Si and Ge phases. *J. Phys.: Condens. Matter* **2002**, *14* (34), 7991–8004.
- (30) Dünner, J.; Mewis, A.  $Ba_8Cu_{16}P_{30}$  eine neue ternäre Variante des Clathrat I-Strukturtyps. Z. Anorg. Allg. Chem. **1995**, 621 (2), 191–196.
- (31) Fulmer, J.; Lebedev, O. I.; Roddatis, V. V.; Kaseman, D. C.; Sen, S.; Dolyniuk, J.-A.; Lee, K.; Olenev, A. V.; Kovnir, K. Clathrate  $Ba_8Au_{16}P_{30}$ : The "Gold Standard" for Lattice Thermal Conductivity. *J. Am. Chem. Soc.* **2013**, *135* (33), 12313–12323.
- (32) Dolyniuk, J.-A.; Wang, J.; Lee, K.; Kovnir, K. Twisted Kelvin Cells and Truncated Octahedral Cages in the Crystal Structures of Unconventional Clathrates,  $AM_2P_4$  (A = Sr, Ba; M = Cu, Ni). *Chem. Mater.* **2015**, 27 (12), 4476–4484.
- (33) Wang, J.; Lebedev, O. I.; Lee, K.; Dolyniuk, J.-A.; Klavins, P.; Bux, S.; Kovnir, K. High-efficiency thermoelectric  $Ba_8Cu_{14}Ge_6P_{26}$ : bridging the gap between tetrel-based and tetrel-free clathrates. *Chem. Sci.* **2017**, 8 (12), 8030–8038.
- (34) Dolyniuk, J.; Whitfield, P. S.; Lee, K.; Lebedev, O. I.; Kovnir, K. Controlling superstructural ordering in the clathrate-I  $Ba_8M_{16}P_{30}$  (M = Cu, Zn) through the formation of metal–metal bonds. *Chem. Sci.* **2017**, 8 (5), 3650–3659.
- (35) Dolyniuk, J.-A.; Wang, J.; Marple, M. A. T.; Sen, S.; Cheng, Y.; Ramirez-Cuesta, A. J.; Kovnir, K. Chemical Bonding and Transport Properties in Clathrates-I with Cu–Zn–P Frameworks. *Chem. Mater.* **2018**, *30* (10), 3419–3428.
- (36) Wang, J.; He, Y.; Mordvinova, N. E.; Lebedev, O. I.; Kovnir, K. The Smaller the Better: Hosting Trivalent Rare-Earth Guests in Cu–P Clathrate Cages. *Chem.* **2018**, *4* (6), 1465–1475.
- (37) Dolyniuk, J.-A.; Zaikina, J. V.; Kaseman, D. C.; Sen, S.; Kovnir, K. Breaking the Tetra-Coordinated Framework Rule: New Clathrate  $Ba_8M_{24}P_{28+\delta}$  (M=Cu/Zn). *Angew. Chem., Int. Ed.* **2017**, *56* (9), 2418–2422.

- (38) Wang, J.; Dolyniuk, J.-A.; Kovnir, K. Unconventional Clathrates with Transition Metal—Phosphorus Frameworks. *Acc. Chem. Res.* **2018**, *51* (1), 31–39.
- (39) Liu, Y.; Wu, L.-M.; Li, L.-H.; Du, S.-W.; Corbett, J. D.; Chen, L. The Antimony-Based Type I Clathrate Compounds Cs<sub>8</sub>Cd<sub>18</sub>Sb<sub>28</sub> and Cs<sub>8</sub>Zn<sub>18</sub>Sb<sub>28</sub>. Angew. Chem. **2009**, 121 (29), 5409–5412.
- (40) He, H.; Zevalkink, A.; Gibbs, Z. M.; Snyder, G. J.; Bobev, S. Synthesis, Structural Characterization, and Physical Properties of the Type-I Clathrates  $A_8Zn_{18}As_{28}$  (A = K, Rb, Cs) and  $Cs_8Cd_{18}As_{28}$ . Chem. Mater. **2012**, 24 (18), 3596–3603.
- (41) Wei, K.; Khabibullin, A. R.; Hobbis, D.; Wong-Ng, W.; Chang, T.; Wang, S. G.; Levin, I.; Chen, Y.-S.; Woods, L. M.; Nolas, G. S. Synthesis, Structure, and Electrical Properties of the Single Crystal Ba<sub>8</sub>Cu<sub>16</sub>As<sub>30</sub>. *Inorg. Chem.* **2018**, *57* (15), 9327–9334.
- (42) Dolyniuk, J.-A.; Owens-Baird, B.; Wang, J.; Zaikina, J. V.; Kovnir, K. Clathrate thermoelectrics. *Mater. Sci. Eng., R* **2016**, *108*, 1–46.
- (43) Cordero, B.; Gomez, V.; Platero-Prats, A. E.; Reves, M.; Echeverria, J.; Cremades, E.; Barragan, F.; Alvarez, S. Covalent radii revisited. *Dalton Trans.* **2008**, No. 21, 2832–2838.
- (44) Cordier, G.; Ochmann, H. Crystal structure of disodium phyllotriantimonidodiindate, Na<sub>2</sub>In<sub>2</sub>Sb<sub>3</sub>. Z. Kristallogr. Cryst. Mater. **1991**, 197, 281.
- (45) Cordier, G.; Ochmann, H. Crystal structure of dipotassium phyllotriantimonidodiindate, K<sub>2</sub>In<sub>2</sub>Sb<sub>3</sub>. *Z. Kristallogr. Cryst. Mater.* **1991**, 197, 293.
- (46) Gourdon, O.; Boucher, F.; Gareh, J.; Evain, M.; O'Connor, C.; Jin-Seung, J. Rubidium Indium Antimonide, Rb<sub>2</sub>In<sub>2</sub>Sb<sub>3</sub>. *Acta Crystallogr., Sect. C: Cryst. Struct. Commun.* **1996**, 52 (12), 2963–2964.
- (47) Blase, W.; Cordier, G.; Somer, M. Crystal structure of decapotassium nonaantimonidopentaindate, K<sub>10</sub>In<sub>5</sub>Sb<sub>9</sub>. *Z. Kristallogr. Cryst. Mater.* **1993**, 203, 146–147.
- (48) Pan, M.-Y.; Xia, S.-Q.; Tao, X.-T. Crystal structure of Ba<sub>5</sub>In<sub>4</sub>Sb<sub>6</sub>. Acta Crystallogr. E **2015**, 71 (5), i4.
- (49) Liu, C.; Tkachenko, N. V.; Popov, I. A.; Fedik, N.; Min, X.; Xu, C.-Q.; Li, J.; McGrady, J. E.; Boldyrev, A. I.; Sun, Z.-M. Structure and Bonding in [Sb@In<sub>8</sub>Sb<sub>12</sub>]<sup>3-</sup> and [Sb@In<sub>8</sub>Sb<sub>12</sub>]<sup>5-</sup>. *Angew. Chem., Int. Ed.* **2019**, *58* (25), 8367–8371.
- (50) Carrillo-Cabrera, W.; Budnyk, S.; Prots, Y.; Grin, Y. Ba<sub>8</sub>Ge<sub>43</sub> revisited: a 2a'×2a'×2a' Superstructure of the Clathrate-I Type with Full Vacancy Ordering. *Z. Anorg. Allg. Chem.* **2004**, *630* (13–14), 2267–2276.
- (51) Dubois, F.; Fässler, T. F. Ordering of Vacancies in Type-I Tin Clathrate: Superstructure of  $Rb_8Sn_{44}$ \_2. *J. Am. Chem. Soc.* **2005**, 127 (10), 3264–3265.
- (52) Kaltzoglou, A.; Fässler, T.; Christensen, M.; Johnsen, S.; Iversen, B.; Presniakov, I.; Sobolev, A.; Shevelkov, A. Effects of the order—disorder phase transition on the physical properties of  $A_8Sn_{44}$  (A = Rb, Cs). *J. Mater. Chem.* **2008**, *18* (46), 5630–5637.
- (53) Kaltzoglou, A.; Hoffmann, S. D.; Fässler, T. F. Order-Disorder Phase Transition in Type-I Clathrate Cs<sub>8</sub>Sn<sub>44</sub>□<sub>2</sub>. *Eur. J. Inorg. Chem.* **2007**, 2007 (26), 4162–4167.
- (54) Zaikina, J. V.; Kovnir, K.; Burkhardt, U.; Schnelle, W.; Haarmann, F.; Schwarz, U.; Grin, Yu.; Shevelkov, A. V. Cationic Clathrate I  $Si_{46-x}P_xTe_y$  (6.6(1)  $\leq y \leq 7.5(1)$ ,  $x \leq 2y$ ): Crystal Structure, Homogeneity Range, and Physical Properties. *Inorg. Chem.* **2009**, *48*, 3720–3730.
- (55) Zaikina, J. V.; Kovnir, K.; Haarmann, F.; Schnelle, W.; Burkhardt, U.; Borrmann, H.; Schwarz, U.; Grin, Yu.; Shevelkov, A. V.  $Si_{172-x}P_xTe_y$  (x=2y, y>20) The First Silicon-Based Cationic Clathrate III with High Thermal Stability. *Chem. Eur. J.* **2008**, *14*, 5414–5422.
- (56) Zaikina, J. V.; Mori, T.; Kovnir, K.; Teschner, D.; Senyshyn, A.; Schwarz, U.; Grin, Yu.; Shevelkov, A. V. Bulk and surface structure and high temperature thermoelectric properties of inverse clathrate-III in the Si-P-Te system. *Chem. Eur. J.* **2010**, *16*, 12582–12589.

- (57) Müller, U. Symmetry Relationships between Crystal Structures: Applications of Crystallographic Group Theory in Crystal Chemistry; Oxford University Press, 2013.
- (58) Chakoumakos, B. C.; Sales, B. C.; Mandrus, D. G. Structural disorder and magnetism of the semiconducting clathrate Eu<sub>8</sub>Ga<sub>16</sub>Ge<sub>30</sub>. *J. Alloys Compd.* **2001**, 322 (1), 127–134.
- (59) Chakoumakos, B. C.; Sales, B. C.; Mandrus, D. G.; Nolas, G. S. Structural disorder and thermal conductivity of the semiconducting clathrate Sr<sub>8</sub>Ga<sub>16</sub>Ge<sub>30</sub>. *J. Alloys Compd.* **2000**, 296 (1), 80–86.
- (60) Okamoto, N. L.; Kim, J.-H.; Tanaka, K.; Inui, H. Splitting of guest atom sites and lattice thermal conductivity of type-I and type-III clathrate compounds in the Ba-Ga-Ge system. *Acta Mater.* **2006**, *54* (20), 5519–5528.
- (61) Sales, B. C.; Chakoumakos, B. C.; Jin, R.; Thompson, J. R.; Mandrus, D. Structural, magnetic, thermal, and transport properties of  $X_8Ga_{16}Ge_{30}$  (X = Eu, Sr, Ba) single crystals. *Phys. Rev. B: Condens. Matter Mater. Phys.* **2001**, 63 (24), 245113.
- (62) Cordier, G.; Ochmann, H. Crystal structure of dirubidium catenadiantimonidogallate, Rb<sub>2</sub>GaSb<sub>2</sub>. *In Z. Kristallogr. Cryst. Mater.* **1991**, *195*, 125.
- (63) Cordier, G.; Orchmann, H. Crystal structure of dicaesium catena-diantimonidogallate, Cs<sub>2</sub>GaSb<sub>2</sub>. Z. Kristallogr. Cryst. Mater. **1991**, 195, 310.
- (64) Blase, W.; Cordier, G.; Somer, M. Crystal structure of hexacaesium triantimonidogallate, Cs<sub>6</sub>InSb<sub>3</sub>. Zeitschrift für Kristallographie 1992, 199, 277.
- (65) Cordier, G.; Ochmann, H.; Schäfer, H. Na<sub>2</sub>Ga<sub>3</sub>Sb<sub>3</sub>, eine neue zintlphase mit schichtstruktur. *Mater. Res. Bull.* **1986**, 21 (3), 331–336.
- (66) Bauer, E. D.; lebarski, A.; Frederick, N. A.; Yuhasz, W. M.; Maple, M. B.; Cao, D.; Bridges, F.; Giester, G.; Rogl, P. Investigation of ferromagnetic filled skutterudite compounds EuT<sub>4</sub>Sb<sub>12</sub>(T = Fe, Ru, Os). *J. Phys.: Condens. Matter* **2004**, *16* (28), 5095–5107.
- (67) Nasir, N.; Grytsiv, A.; Rogl, P.; Saccone, A.; Giester, G. Phase equilibria in systems Ce–M–Sb (M=Si, Ge, Sn) and superstructure  $Ce_{12}Ge_{9-x}Sb_{23+x}$  (x=3.8 $\pm$ 0.1). *J. Solid State Chem.* **2009**, 182 (4), 645–656.
- (68) Saparov, B.; Bobev, S.; Ozbay, A.; Nowak, E. R. Synthesis, structure and physical properties of the new Zintl phases  $Eu_{11}Zn_6Sb_{12}$  and  $Eu_{11}Zd_6Sb_{12}$ . J. Solid State Chem. **2008**, 181 (10), 2690–2696.
- (69) Poth, L. Bauprinzipien isolierter intermetallischer Moleküle. Eine massenzweispektrometrische Studie. Dissertation, TH-Darmstadt, 1993.
- (70) Vinet, P.; Ferrante, J.; Rose, J. H.; Smith, J. R. Compressibility of solids. *J. Geophys. Res.* **1987**, 92 (B9), 9319–9325.
- (71) Zollner, S.; Gopalan, S.; Cardona, M. The temperature dependence of the band gaps in InP, InAs, InSb, and GaSb. *Solid State Commun.* **1991**, 77 (7), 485–488.
- (72) Kim, Y.-S.; Marsman, M.; Kresse, G.; Tran, F.; Blaha, P. Towards efficient band structure and effective mass calculations for III-V direct band-gap semiconductors. *Phys. Rev. B: Condens. Matter Mater. Phys.* **2010**, 82 (20), 205212.
- (73) Iversen, B. B.; Palmqvist, A. E. C.; Cox, D. E.; Nolas, G. S.; Stucky, G. D.; Blake, N. P.; Metiu, H. Why are Clathrates Good Candidates for Thermoelectric Materials? *J. Solid State Chem.* **2000**, 149 (2), 455–458.
- (74) Qiu, L.; Swainson, I. P.; Nolas, G. S.; White, M. A. Structure, thermal, and transport properties of the clathrates  $Sr_8Zn_8Ge_{38}$ ,  $Sr_8Ga_{16}Ge_{30}$ , and  $Ba_8Ga_{16}Si_{30}$ . Phys. Rev. B: Condens. Matter Mater. Phys. **2004**, 70 (3), No. 035208.
- (75) The Physics and Chemistry of Inorganic Clathrates; Nolas, G. S., Ed.; Springer: New York, 2014.
- (76) Du, B.; Saiga, Y.; Kajisa, K.; Takabatake, T. Thermoelectric performance of Zn-substituted type-VIII clathrate Ba<sub>8</sub>Ga<sub>16</sub>Sn<sub>30</sub> single crystals. *J. Appl. Phys.* **2012**, *111* (1), No. 013707.
- (77) Saiga, Y.; Suekuni, K.; Deng, S. K.; Yamamoto, T.; Kono, Y.; Ohya, N.; Takabatake, T. Optimization of thermoelectric properties of type-VIII clathrate  $Ba_8Ga_{16}Sn_{30}$  by carrier tuning. *J. Alloys Compd.* **2010**, 507 (1), 1–5.

- (78) Suekuni, K.; Avila, M. A.; Umeo, K.; Fukuoka, H.; Yamanaka, S.; Nakagawa, T.; Takabatake, T. Simultaneous structure and carrier tuning of dimorphic clathrate Ba<sub>8</sub>Ga<sub>16</sub>Sn<sub>30</sub>. *Phys. Rev. B: Condens. Matter Mater. Phys.* **2008**, 77 (23), 235119.
- (79) Goldsmid, H. J.; Sharp, J. W. Estimation of the thermal band gap of a semiconductor from seebeck measurements. *J. Electron. Mater.* **1999**, 28 (7), 869–872.
- (80) Deng, S.; Tang, X.; Zhang, Q. Synthesis and thermoelectric properties of p-type  $Ba_8Ga_{16}Zn_xGe_{30-x}$  type-I clathrates. *J. Appl. Phys.* **2007**, *102* (4), No. 043702.
- (81) Zhang, H.; Borrmann, H.; Oeschler, N.; Candolfi, C.; Schnelle, W.; Schmidt, M.; Burkhardt, U.; Baitinger, M.; Zhao, J.-T.; Grin, Y. Atomic Interactions in the p-Type Clathrate I Ba<sub>8</sub>Au<sub>5.3</sub>Ge<sub>40.7</sub>. *Inorg. Chem.* **2011**, *50* (4), 1250–1257.
- (82) Ortiz, B. R.; Gorai, P.; Krishna, L.; Mow, R.; Lopez, A.; McKinney, R.; Stevanović, V.; Toberer, E. S. Potential for high thermoelectric performance in n-type Zintl compounds: a case study of Ba doped KAlSb<sub>4</sub>. *J. Mater. Chem. A* **2017**, *5* (8), 4036–4046.
- (83) Zeier, W. G.; Zevalkink, A.; Schechtel, E.; Tremel, W.; Snyder, G. J. Thermoelectric properties of Zn-doped Ca<sub>3</sub>AlSb<sub>3</sub>. *J. Mater. Chem.* **2012**, 22 (19), 9826–9830.
- (84) Zevalkink, A.; Toberer, E. S.; Zeier, W. G.; Flage-Larsen, E.; Snyder, G. J. Ca<sub>3</sub>AlSb<sub>3</sub>: an inexpensive, non-toxic thermoelectric material for waste heat recovery. *Energy Environ. Sci.* **2011**, 4 (2), 510–518
- (85) Toberer, E. S.; Zevalkink, A.; Crisosto, N.; Snyder, G. J. The Zintl Compound Ca<sub>5</sub>Al<sub>2</sub>Sb<sub>6</sub> for Low-Cost Thermoelectric Power Generation. *Adv. Funct. Mater.* **2010**, 20 (24), 4375–4380.
- (86) Zevalkink, A.; Zeier, W. G.; Pomrehn, G.; Schechtel, E.; Tremel, W.; Snyder, G. J. Thermoelectric properties of Sr<sub>3</sub>GaSb<sub>3</sub> a chain-forming Zintl compound. *Energy Environ. Sci.* **2012**, 5 (10), 9121–9128.
- (87) Hrostowski, H. J.; Morin, F. J.; Geballe, T. H.; Wheatley, G. H. Hall Effect and Conductivity of InSb. *Phys. Rev.* **1955**, *100* (6), 1672–1676
- (88) Oszwalldowski, M.; Zimpel, M. Temperature dependence of intrinsic carrier concentration and density of states effective mass of heavy holes in InSb. J. Phys. Chem. Solids 1988, 49 (10), 1179–1185.
- (89) Weippert, V.; Haffner, A.; Stamatopoulos, A.; Johrendt, D. Supertetrahedral Layers Based on GaAs or InAs. J. Am. Chem. Soc. 2019, 141 (28), 11245–11252.
- (90) Caillat, T.; Borshchevsky, A.; Fleurial, J. P. Properties of single crystalline semiconducting CoSb<sub>3</sub>. *J. Appl. Phys.* **1996**, *80* (8), 4442–4449.
- (91) Chung, D.-Y.; Hogan, T.; Brazis, P.; Rocci-Lane, M.; Kannewurf, C.; Bastea, M.; Uher, C.; Kanatzidis, M. G. CsBi<sub>4</sub>Te<sub>6</sub>: A High-Performance Thermoelectric Material for Low-Temperature Applications. *Science* **2000**, 287 (5455), 1024–1027.
- (92) Watcharapasorn, A.; DeMattei, R. C.; Feigelson, R. S.; Caillat, T.; Borshchevsky, A.; Snyder, G. J.; Fleurial, J.-P. Preparation and thermoelectric properties of some phosphide skutterudite compounds. *J. Appl. Phys.* **1999**, *86* (11), 6213–6217.